Available online at www.sciencedirect.com
ScienceDirect
Journal of Sound and Vibration 306 (2007) 564–579
JOURNAL OF SOUND AND VIBRATION
www.elsevier.com/locate/jsvi

Aerodynamic noise prediction for long-span bodies

Jung H. Seo, Young J. Moon*

Department of Mechanical Engineering, Korea University, Seoul 136-701, Korea

Received 21 June 2006; received in revised form 19 May 2007; accepted 27 May 2007
Available online 24 July 2007

Abstract

A computational methodology is proposed for aerodynamic noise prediction of long-span bodies at low Mach numbers. The three-dimensional hydrodynamic field is computed by incompressible large eddy simulation, while its two-dimensional acoustic field at zero spanwise wavenumber is solved by the linearized perturbed compressible equations (LPCE). A far-field acoustic pressure is obtained by extrapolating the pressure fluctuations with Kirchhoff method, followed by a three-dimensional correction with Oberai et al.'s formula. The far-field sound pressure level for the long span is then estimated by a correction method, which is formally derived by revisiting the previous works of Kato et al. and Perot et al., along with discussion on finding the spanwise coherence lengths. The accuracy of the present method is assessed for broadband noise (with a broadened tone) from a flow with $Re_D = 4.6 \times 10^4$ and $M = 0.21$, past a circular cylinder of 30 cylinder-diameter span. The computed aerodynamic and acoustic results are found in excellent agreement with the experimental measurements.

1. Introduction

A turbulent flow over the long-span body (e.g. circular cylinder, airfoil, flat plate, and forward/backward steps) is often encountered in many aerodynamic analyses. The characteristics of the turbulent flow have extensively been studied by direct numerical simulation (DNS) or large eddy simulation (LES) but its noise prediction at low Mach numbers has been conducted with limited extents. At low Mach numbers, the scale disparity between the turbulent eddies and the acoustic waves becomes so large that direct computation of the flow and sound will be very expensive and difficult.

To overcome this problem, an alternate approach of hybrid methods has been used by several researchers; for example, Lighthill/Curle integral formulation with compressible or incompressible LES solution [1,2] and the linearized Euler equations (LEE) with the source terms extracted from LES solutions [3–5]. The latter is effective but defining the source terms still remains as an open issue. Recently, Ewert and Schröder [6,7] have proposed the acoustic perturbation equations (APE) with the compressible flow as a base solution. This method is based on a source-term filtering technique, which intents to eliminate the vortical and entropy modes from the compressible flow solution.

*Corresponding author.
E-mail address: yjmoon@korea.ac.kr (Y.J. Moon).

0022-460X/$ - see front matter © 2007 Elsevier Ltd. All rights reserved.
doi:10.1016/j.jsv.2007.05.042

In this study, we propose a hybrid method for prediction of turbulent flow noise at low Mach numbers. This method is based on a hydrodynamic/acoustic splitting technique [8–12], an alternative to solve the low Mach number aeroacoustic problems. A turbulent flow is computed by incompressible LES, while the generation and propagation of the acoustic field is predicted by the linearized perturbed compressible equations (LPCE) [12], with the acoustic sources acquired from incompressible LES solution. This LPCE formulation ensures consistent, grid-independent acoustic solutions by suppressing the unstable vortical mode in the perturbed system. The present method is computationally efficient because it is based on an incompressible flow solver and the grid systems for flow and acoustics can be treated differently.

A far-field sound pressure level (SPL) for the long span is calculated by an approximate but efficient computational approach. The far-field acoustic pressure is obtained by extrapolating the pressure fluctuations with Kirchhoff method [13], followed by a three-dimensional correction with Oberai et al.'s formula [14]. The far-field SPL for the long span is then estimated by a correction method, which is formally derived by revisiting the previous works of Kato et al. [15] and Perot et al. [2].

In the present study, the afore-mentioned computational methods are validated for broadband noise (with a broadened tone) from a flow with $Re_D = 4.6 \times 10^4$ and $M = 0.21$, past a circular cylinder of 30 cylinder-diameter span. The computed aerodynamic and acoustic results are compared with the experimentally measured data [1,16,24], along with discussion on finding the spanwise coherence lengths. In addition, a relation is derived between the spanwise coherence function of the far-field acoustic pressure emitted from the body surface and that of the integrated surface pressure.

In Section 2, the computational methodologies and numerical schemes are described for LES, LPCE, and the far-field SPL prediction methods. The computed aerodynamic and acoustic results are presented in Section 3, with discussion on the accuracy of the computed spanwise coherence lengths and its sensitivity to the amount of SPL correction for the long span.

2. Computational methodologies

2.1. Incompressible LES/LPCE hybrid method

The aerodynamic noise prediction for the long-span bodies starts with computing a low Mach number turbulent flow by incompressible LES. This is based on the hydrodynamic/acoustic splitting method [8–12], in which the total flow variables are decomposed into the incompressible and perturbed compressible variables as:

$$\begin{aligned} \rho(\vec{x},t) &= \rho_0 + \rho'(\vec{x},t), \\ \vec{u}(\vec{x},t) &= \vec{U}(\vec{x},t) + \vec{u}'(\vec{x},t), \\ p(\vec{x},t) &= P(\vec{x},t) + p'(\vec{x},t). \end{aligned} \tag{1}$$

The incompressible variables represent hydrodynamic turbulent flow field, while acoustic fluctuations and other compressibility effects are resolved by perturbed quantities denoted by ($'$).

The filtered incompressible Navier–Stokes equations are written as

$$\frac{\partial \tilde{U}_j}{\partial x_j} = 0, \tag{2}$$

$$\rho_0 \frac{\partial \tilde{U}_i}{\partial t} + \rho_0 \frac{\partial}{\partial x_j}(\tilde{U}_i \tilde{U}_j) = -\frac{\partial \tilde{P}}{\partial x_i} + \mu_0 \frac{\partial}{\partial x_j}\left(\frac{\partial \tilde{U}_i}{\partial x_j} + \frac{\partial \tilde{U}_j}{\partial x_i}\right) - \rho_0 \frac{\partial}{\partial x_j} M_{ij}, \tag{3}$$

where the grid-resolved quantities are denoted by ($\tilde{}$) and the unknown sub-grid tensor M_{ij} is modeled as

$$M_{ij} = \widetilde{U_i U_j} - \tilde{U}_i \tilde{U}_j = -(C_s \Delta)^2 |\tilde{S}| \tilde{S}_{ij}. \tag{4}$$

Here, Δ is a mean radius of the grid cell (computed as cubic root of its volume).

After a quasi-periodic stage of hydrodynamic field is attained, the perturbed quantities are computed by the LPCE. A set of the LPCEs is written in a vector form as:

$$\frac{\partial \rho'}{\partial t} + (\vec{U} \cdot \nabla)\rho' + \rho_0(\nabla \cdot \vec{u}') = 0 \tag{5}$$

$$\frac{\partial \vec{u}'}{\partial t} + \nabla(\vec{u}' \cdot \vec{U}) + \frac{1}{\rho_0}\nabla p' = 0 \tag{6}$$

$$\frac{\partial p'}{\partial t} + (\vec{U} \cdot \nabla)p' + \gamma P(\nabla \cdot \vec{u}') + (\vec{u}' \cdot \nabla)P = -\frac{\mathrm{D}P}{\mathrm{D}t}. \tag{7}$$

The left-hand side of LPCE represents effects of acoustic wave propagation and refraction in an unsteady, inhomogeneous flow, while the right-hand side only contains an acoustic source term, which is projected from the hydrodynamic flow solution. It is interesting to note that for low Mach number flows, the total change of the hydrodynamic pressure, $\mathrm{D}P/\mathrm{D}t$ is considered as the only explicit noise source term.

Because a curl of the linearized perturbed momentum equations, Eq. (6) yields

$$\frac{\partial \vec{\omega}'}{\partial t} = 0, \tag{8}$$

LPCE prevents any further changes (generation, convection, and decaying) of perturbed vorticity in time. In fact, the perturbed vorticity ($\vec{\omega}' = \nabla \times \vec{u}'$) could yield self-excited errors, if $\vec{\omega}'$ is not properly resolved with the acoustic grid. Hence, the evolution of the perturbed vorticity is pre-suppressed in LPCE, deliberating the fact that the perturbed vorticity has little effects on the noise generation, particularly at low Mach numbers. For hybrid methods, this is an important property that ensures consistent, grid-independent acoustic solutions. The LPCE has been validated for a laminar tone from a circular cylinder at $Re_D = 150$ and $M = 0.1$ and also for the vortex sound problems at higher Reynolds numbers, i.e. quadruple sound of Kirchhoff vortex and temporal mixing layer noise. Details on the derivation of LPCE and the characteristics of the perturbed vorticity can be found in Ref. [12].

The filtered incompressible Navier–Stokes equations are solved by an iterative fractional-step method, and the LPCEs are solved in a time-marching fashion. The governing equations are spatially discretized with a sixth-order compact scheme [18] to avoid excessive numerical dissipations and dispersions errors and integrated in time by a four-stage Runge–Kutta method. A tenth-order spatial filtering (cut-off wavenumber, $k\Delta x \approx 2.9$) proposed by Gaitonde et al. [19] is also employed to enhance the numerical stability. This filtering will be discussed more in Section 3 with the sub-grid scale (SGS) model used in LES.

2.2. Computation of far-field acoustics

In the present study, we are concerned with a low Mach number turbulent flow, which is statistically homogeneous in the spanwise direction over the long span. In incompressible LES, a spanwise periodic boundary condition allows to capture the spanwise-correlated flow structure with a short simulated span (L_s). In LPCE calculation, however, applying periodic boundary condition to the same spanwise width will result in un-physically correlated acoustic result [2,7,20] because the acoustic wavelength is usually much larger than the turbulence length scales. To avoid this matter, one must either use a very long span that fully covers the acoustic correlation length or apply an absorbing boundary condition at the spanwise boundaries. The former is hardly possible for any case. The latter is not possible for DNS but will be an easy task for the present hybrid method because the spanwise boundary conditions for the flow and acoustics can be treated differently.

In this study, an approximated but computationally efficient approach is pursued. Instead of solving 3D LPCE with absorbing boundary condition applied at the spanwise boundaries [21], a two-dimensional acoustic field at zero spanwise wavenumber, $k_z = 0$ is calculated in the mid-span plane, with acoustic sources and hydrodynamic variables integrated in the spanwise direction;

$$\bar{q}(x, y, t) = \int_0^{L_s} q(x, y, z, t)\,\mathrm{d}z, \tag{9}$$

where L_s is the span used in 3D flow simulation. In 3D aero-acoustics, it is important to note that the strength of the noise source is directly related to the spanwise coherence length scale of the flow. In fact, Eq. (9) has already taken this into account for those scales resolved within L_s. The computed far-field acoustic pressure is then corrected by the following relation. Considering an acoustic wave equation which is Fourier-transformed in the spanwise direction, a three-dimensionally radiated far-field acoustic pressure in frequency domain, $\hat{p}'$ is related to the two-dimensionally predicted acoustic pressure at $k_z = 0$, $\bar{\hat{p}}'$ by

$$\hat{p}'(x, y, 0, \omega) \approx \bar{\hat{p}}'(x, y, \omega) \frac{1+i}{2} \sqrt{\frac{\omega}{c_o \pi r}}, \tag{10}$$

where c_o is the ambient speed of sound. Derivation of this relation proposed by Oberai et al. may be found in Ref. [14].

At low Mach numbers, acoustic waves generated in the stream of turbulences have a range of wavelengths, all of which are difficult to be resolved unless grids are really fine up to the far-field boundaries. If an observer's position is far from the noise source, an acoustic domain can be truncated and the acoustic pressure obtained by LPCE can be extrapolated from the truncated boundaries to the far-field observer's position by 2D Kirchhoff method [13],

$$4i\hat{p}' = -\int_S \left[\frac{\partial \hat{p}'}{\partial n} H_o^{(2)}(\omega r/c_o) - \frac{\omega}{c_o} (\hat{n} \cdot \hat{r}) \hat{p}' H_1^{(2)}(\omega r/c_o) \right] \mathrm{d}S, \tag{11}$$

where r is the distance from the source to the observer's position, $\hat{n}$ is a unit vector normal to the Kirchhoff surface, and H is the Hankel function. In Eq. (11), the effect of the momentum fluctuations (Lighthill stress tensor) is neglected because the Kirchhoff surface is usually set in the mid-field, where the momentum fluctuations are almost negligible.

2.3. Estimation of far-field SPL for the long span

In order to estimate a SPL for the long span (L), SPL for the simulated span (L_s) must be corrected. According to Kato et al. [15], SPL correction for the long span can be made by adding $10\log(L/L_s)$, if a coherence length of the surface pressure fluctuations, L_C is determined less than the simulated span, i.e. $L_C \leqslant L_s$. If $L_C > L$ (i.e. for nearly planar waves), $20\log(L/L_s)$ must be added. This simple correction has been used for various studies [1,7,20,22]. Although two asymptotic values are correct, Kato's method is rather ad hoc, when $L_s \leqslant L_C \leqslant L$. Recently, Perot et al. [2] proposed a more elaborated correction method, considering an acoustic spanwise coherence function with the Curle's analogy solution. This method may give a more realistic result in the near-field because a retarded time is taken into account. But the methodology has not been completed for practical use.

In this study, we propose a correction method, revisiting the previous works of Kato et al. [15] and Perot et al. [2]. First, consider a long-span body, which is divided into N subsections by L_s (i.e. $L = NL_s$) because the acoustic pressure radiated from the simulated span, L_s is the only known solution (see Fig. 1). Let the spectral acoustic pressure radiated from the i-th subsection be $\hat{p}'_i$, then the power spectral density of the acoustic pressure for entire span, $\hat{p}'_L$ can be written as

$$\hat{p}'_L \hat{p}'^*_L = \sum_{i=1}^{N} \hat{p}'_i \sum_{j=1}^{N} \hat{p}'^*_j = \sum_{i=1}^{N} \sum_{j=1}^{N} \mathrm{Re}(\hat{p}'_i \hat{p}'^*_j), \tag{12}$$

where * denotes a conjugate.

Now, we need an assumption of '*statistical homogeneity in the spanwise direction*' that satisfies the following properties of simulated span, L_s.

1. The power spectral density of the acoustic pressure radiated from each subsection is the same, i.e.

$$|\hat{p}'_1|^2 = |\hat{p}'_2|^2 = \cdots = |\hat{p}'_N|^2 = |\hat{p}'_s|^2, \tag{13}$$

where $\hat{p}'_s$ is the spectral acoustic pressure radiated from L_s.

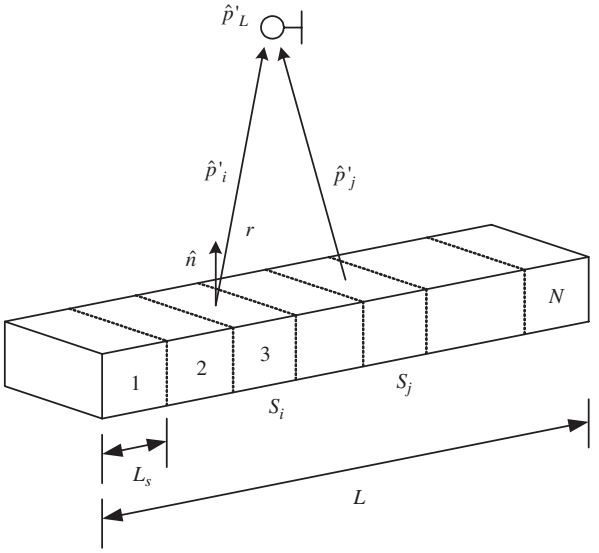

Fig. 1. Schematic of a long-span body divided by N subsections.

2. The acoustic pressure radiated from each subsection is only lagged by a phase difference which can be characterized by the following coherence function,

$$\gamma'_{ij} = \frac{\overline{\mathrm{Re}(\hat{p}'_i \hat{p}'^{*}_j)}}{\sqrt{|\hat{p}'_i|^2}\sqrt{|\hat{p}'_j|^2}}. \tag{14}$$

This function will be simply named an '*acoustic spanwise coherence function*' from hereafter.

3. The above coherence function (phase lagging) is a function of Δz_{ij}, the spanwise separation between two subsections:

$$\gamma'_{ij} = \gamma'(\Delta z_{ij}), \quad \Delta z_{ij} = |z_i - z_j| = |i-j|L_s. \tag{15}$$

In many cases, these assumptions are not so crude, if the observer's position is sufficiently far. By employing Eqs. (13)–(15), the power spectral density of the acoustic pressure emitted from the entire span, Eq. (12) can be written as

$$|\hat{p}'_L|^2 = \sum_{i=1}^{N}\sum_{j=1}^{N} \gamma'(\Delta z_{ij})|\hat{p}'_s|^2. \tag{16}$$

So, one can now estimate $|\hat{p}'_L|^2$ by determining $\gamma'(\Delta z_{ij})$. Since the phase lagging in the spanwise direction tends to follow a Gaussian distribution [23,24], the acoustic spanwise coherence function, $\gamma'(\Delta z_{ij})$ can be expressed as

$$\gamma'(\Delta z_{ij}) = \exp\left(-\frac{\Delta z_{ij}^2}{L'_c(\omega)^2}\right), \tag{17}$$

where $L'_c(\omega)$ is the spanwise coherence length, which is also a function of frequency. Note that $L'_c(\omega)$ is different from $L_C(\omega)$ in the earlier work of Kato et al. [15].

From Eqs. (16) and (17), SPL to be corrected for the long span, L is given by

$$\begin{aligned}\mathrm{SPL}_c(\omega) &= 10\log\left(\frac{|\hat{p}'_L(\omega)|^2}{|\hat{p}'_s(\omega)|^2}\right)\\ &= 10\log\left(\sum_{i=1}^{N}\sum_{j=1}^{N}\exp\left(-(i-j)^2\left(\frac{L_s}{L'_c(\omega)}\right)^2\right)\right).\end{aligned} \tag{18}$$

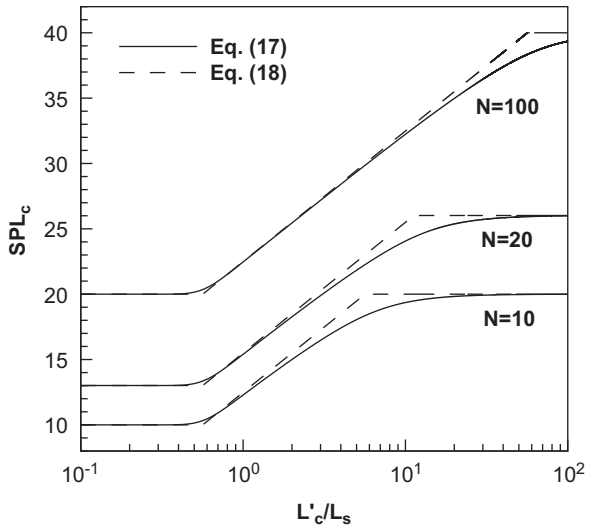

Fig. 2. SPL correction for the long span.

Eq. (18) is plotted in Fig. 2 (solid lines) against L_c'/L_s for various $N(=L/L_s)$. If $L_c'/L_s<1/\sqrt{\pi}(\approx 0.56)$, $\mathrm{SPL}_c(\omega)$ converges to $10\log(N)$, while $\mathrm{SPL}_c(\omega)$ approaches to $20\log(N)$, if $L_c'/L_s>N/\sqrt{\pi}$ (or $L_c'>L/\sqrt{\pi}$). When N is sufficiently large, SPL_c is linearly proportional to $\log(L_c'/L_s)$ in the range of $1/\sqrt{\pi}<L_c'/L_s<N/\sqrt{\pi}$. Therefore, Eq. (18) can be approximated to a simpler form (dashed lines), which might be useful in engineering purposes:

$$\mathrm{SPL}_c=\begin{cases}10\log(N) & (L_c'/L_s\leqslant 1/\sqrt{\pi}),\\ 10\log(L_c'/L_s)+10\log(\sqrt{\pi}N) & (1/\sqrt{\pi}<L_c'/L_s<N/\sqrt{\pi}),\\ 20\log(N) & (L_c'/L_s\geqslant N/\sqrt{\pi}).\end{cases} \tag{19}$$

It is interesting to note that Eq. (18) or (19) has the same asymptotic behavior as Kato's formula and also that Eq. (19) can be still useful for small N, as long as L_c'/L_s is not too large, for example, less than 3.

As shown above, determining $L_c'(\omega)$ from the acoustic spanwise coherence function, $\gamma'(\Delta z_{ij})$ is an important step for estimating $\mathrm{SPL}_c(\omega)$. Actually, $\gamma'(\Delta z_{ij})$ is the spanwise coherence function of the acoustic pressure radiated from each subsection surface, whereas experimentally measuring that is hardly possible because the acoustic far-field cannot be windowed (or sectioned) by L_s for the entire span. Alternatively, it can be estimated by an acoustic analogy with the computed (or measured) surface pressure data [2]. The cross power spectrum $\hat{p}_i'\hat{p}_j'^{*}$ can be evaluated with the surface pressure, using Curle's analogy solution:

$$\hat{p}'(\omega)\simeq\frac{1}{4\pi c_0}\int(\vec{r}\cdot\hat{n})(-\mathrm{i}\omega\hat{P}(\omega))\exp(\mathrm{i}\omega r/c_0)\,\mathrm{d}S. \tag{20}$$

For a compact source or when observer's position is very far, it can be assumed that $r/c_0\approx$ constant. Then, the cross power spectrum $\hat{p}_i'\hat{p}_j'^{*}$ is analytically written as

$$\hat{p}_i'\hat{p}_j'^{*}\simeq\left|\frac{-\mathrm{i}\omega\exp(\mathrm{i}\omega r/c_0)}{4\pi c_0}\right|^2\int(\vec{r}\cdot\hat{n})\hat{P}_i\,\mathrm{d}S_i\int(\vec{r}\cdot\hat{n})\hat{P}_j^{*}\,\mathrm{d}S_j \tag{21}$$

and Eq. (14) can be expressed as

$$\gamma'(\Delta z_{ij})\simeq\frac{\overline{\mathrm{Re}\left(\int(\vec{r}\cdot\hat{n})\ \hat{P}_i\,\mathrm{d}S_i\int(\vec{r}\cdot\hat{n})\hat{P}_j^{*}\,\mathrm{d}S_j\right)}}{\sqrt{|\int(\vec{r}\cdot\hat{n})\,\hat{P}_i\,\mathrm{d}S_i|^2}\sqrt{|\int(\vec{r}\cdot\hat{n})\,\hat{P}_j\,\mathrm{d}S_j|^2}}, \tag{22}$$

where $\hat{P}_i$ is the surface pressure at each subsection and $\int \mathrm{d}S_i$ is the surface integral over each subsectional area. Eq. (22) is a relation between the acoustic spanwise coherence function, $\gamma'(\Delta z_{ij})$ and the spanwise coherence function of the 'integrated' surface pressure. For a certain application, it is also possible to replace $\gamma'(\Delta z_{ij})$ by the spanwise coherence function of the surface pressure at a point of interest, and such a coherence function can be easily computed or measured by experiments.

3. Results and discussion

The proposed aerodynamic noise prediction method for the long-span bodies is validated for broadband noise (with a broadened tone) from a flow past a circular cylinder of 30 cylinder-diameter span (see Fig. 3). The flow is at $Re_D = 4.6 \times 10^4$ and $M = 0.21$ (a sub-critical regime), where a dipole-tone is broadened by the spanwise instability of the shear layer emanated from the separated boundary layer at the cylinder surface. The computed aerodynamic and acoustic results will be compared with the experimental measurements [16,1,24], along with discussion on finding the spanwise coherence lengths.

3.1. Flow over the circular cylinder

According to Szepessy's experiment [17], a spanwise correlation length of the cylinder cross flow is found as $2.7D$ at $Re_D = 43000$. So, an incompressible LES is conducted for the span, $L_s = 3D$ with flow periodicity assumed in the spanwise direction (see Fig. 3). An O-type cylindrical grid is used with approximately 10^6 mesh points: $181 \times 181 \times 31$ in the circumferential, radial, and spanwise directions, respectively, and the computational domain is divided into 16 blocks for parallel computation. The minimal grid size adjacent to the wall is $0.005D$ and the time step used in the computation is $0.002tU/D$, which corresponds to the CFL number of 0.4.

In this study, two LESs were conducted with a Smagorinsky model with van Driest damping function at the wall ($C_s = 0.065$) and no SGS model. No significant differences were observed but at least for the global aerodynamic quantities, i.e. Strouhal number and the mean and rms values of C_D and C_L, the latter yielded somewhat better performances. This agrees with the previous study of Visbal and Rizetta [25], who have tested the compact/filtering scheme (same spatial discretization and filtering formula used in the present study) for the isotropic turbulence and the low Reynolds number turbulent channel flow. It has been shown that the tenth-order spatial filtering used in the present study has a cut-off wavenumber, $k\Delta x \approx 2.9$, which far exceeds the test-filter width of $k\Delta x = \pi/2 \approx 1.57$ and therefore only damps out the scales which are un-resolved by the sixth-order spatial differencing scheme. But the present compact/filtering scheme with the standard eddy-viscosity SGS models dissipates energy over a wide range of wavenumbers including the resolved scales. This problem comes from the SGS model that cannot be corrected by simply adjusting the constant in the model

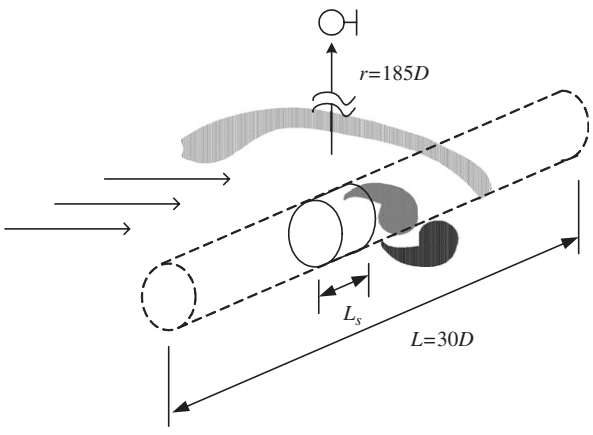

Fig. 3. Schematic of flow-induced noise from a long circular cylinder in cross flow.

[25]. The present LES is therefore performed with no SGS model, but finding a proper turbulence closure model for the compact/filtering LES still remains as an open issue and will be pursued in the future study.

At $\tilde{t} = 100\,t\,U/D$ (U: free-stream velocity), a quasi-periodic stage of the flow is established. After an additional computation for $200\,t\,U/D$, 80 cycles of the von Karman vortex shedding were obtained. The boundary layer at the cylinder surface remains laminar but after separation, the shear layer immediately breaks off into smaller eddies. The iso-surfaces of the second invariant property of the velocity gradient, $Q = (\Omega_{ij}\Omega_{ij} - S_{ij}S_{ij})/2$ (Ω_{ij}&S_{ij}: rotation and strain rate tensors) are plotted in Fig. 4, where a coherent von Karman vortex street and highly three-dimensional wake structures are clearly visualized. Fig. 5(a) shows the time variations of the lift and drag coefficients, oscillating at Strouhal numbers ($St = fh/U$) of 0.19 and 0.38, respectively. The mean pressure coefficient along the cylinder surface is also compared in Fig. 5(b) with the experimental data [16], indicating a fairly good agreement. The back pressure and the lowest peaks are slightly

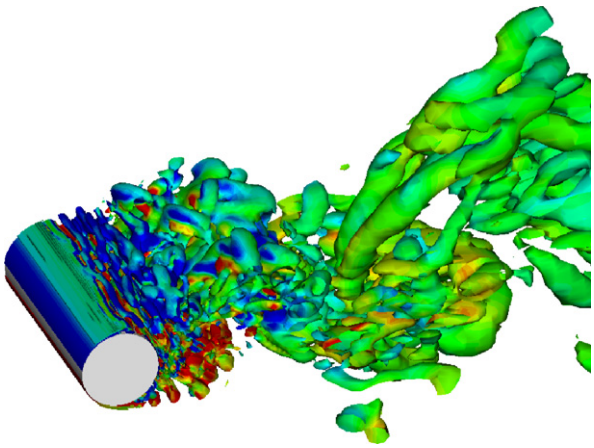

Fig. 4. Three-dimensional flow structures over the circular cylinder at $Re_D = 46000$ and $M = 0.21$; Iso-surface of $Q = 0.5$, non-dimensionalized by $(U_\infty/D)^2$.

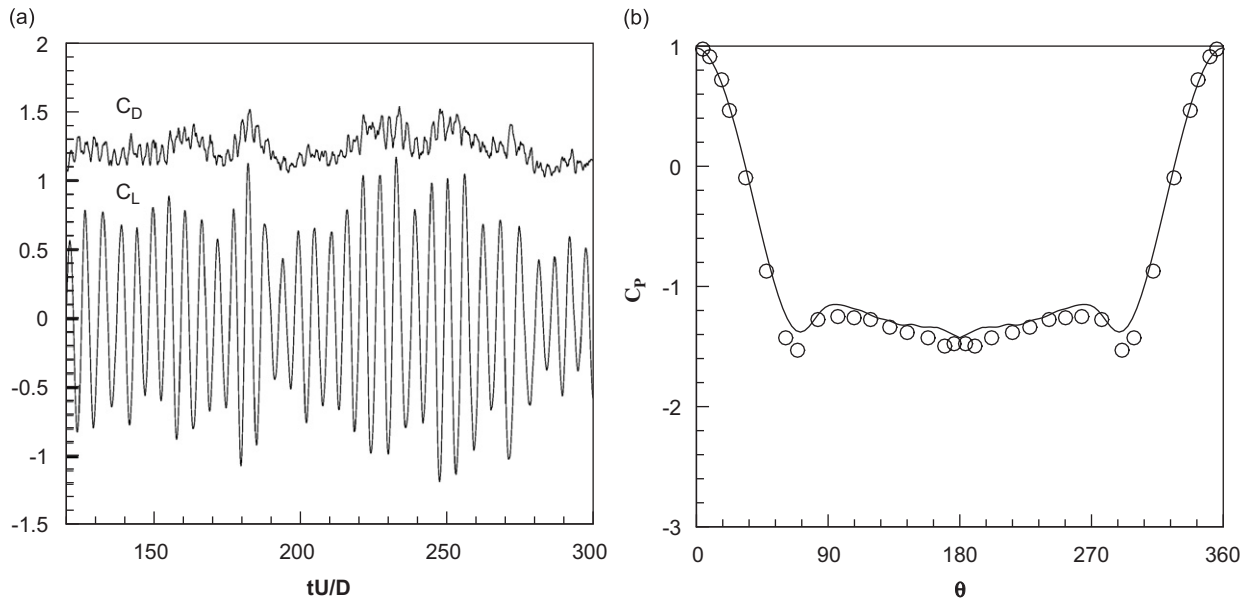

Fig. 5. Aerodynamic characteristics: (a) time variation of lift and drag coefficients; (b) mean pressure coefficient along the cylinder surface; −: present computation, ○: measurement by Szepessy and Bearman [16].

under-predicted but the lowest peak positions seem to be well met. In Table 1, aerodynamic coefficients are also compared with the experimental data of Szepessy and Bearman [16]. The computed Strouhal number is found in good agreement with the experimental measurements. The drag coefficient in rms value is slightly under-predicted but the mean drag coefficient and the rms value of the lift coefficient agree well with the measured data. Some discrepancy may be due to the limited size of the span or issues of turbulence closure model.

The auto-spectra of the pressure fluctuations over the cylinder surface, $\Phi_A(\omega) = \lim_{T\to\infty}(1/T)\hat{P}(\omega)\hat{P}^*(\omega)$ are plotted in Fig. 6 for various circumferential positions ($\theta = 0^\circ$ corresponds to the wake line). Due to the lift fluctuations, a maximum peak is observed at $St = 0.19$ over the cylinder top ($\theta = 90^\circ$). At the wake line, however, peak is at $St = 0.38$ for the drag. One can also notice the pronounced high-frequency fluctuations of the pressure along the cylinder rear at $0.3 < St < 1.2$. These are attributed to the wake turbulences and will be acting as the volume source for the noise generation. Fig. 7(a) and (b) show that $\Phi_A(\omega)$ spectra at $\theta = 90^\circ$ are almost identical along the spanwise direction, while its spanwise phase difference, $\Delta\phi = \arctan(\mathrm{Im}(\Phi_C)/\mathrm{Re}(\Phi_C))$ varies substantially in most of the frequencies, except at $St = 0.19$. From these results, a flow over the circular cylinder may be regarded as statically homogeneous in the spanwise direction. Here, $\Phi_C = \lim_{T\to\infty}(1/T)\hat{P}(\omega, z)\hat{P}^*(\omega, z + \Delta z)$ is the cross spectra of the surface pressure fluctuations at $\theta = 90^\circ$.

3.2. Acoustic field computation (LPCE)

A two-dimensional LPCE computation is conducted with acoustic sources and hydrodynamic variables spanwise-integrated at $k_z = 0$. The acoustic meshes (161×241) are distributed in the circumferential and radial directions over the circular domain, which is radially extended up to $r = 80D$. In this problem, acoustic

Table 1
Aerodynamic coefficients

	St	$C_{D,\mathrm{avg}}$	$C_{D,\mathrm{rms}}$	$C_{L,\mathrm{rms}}$
Present	0.187	1.24	0.1	0.54
Experiment	0.19	1.35	0.16	0.45–0.5

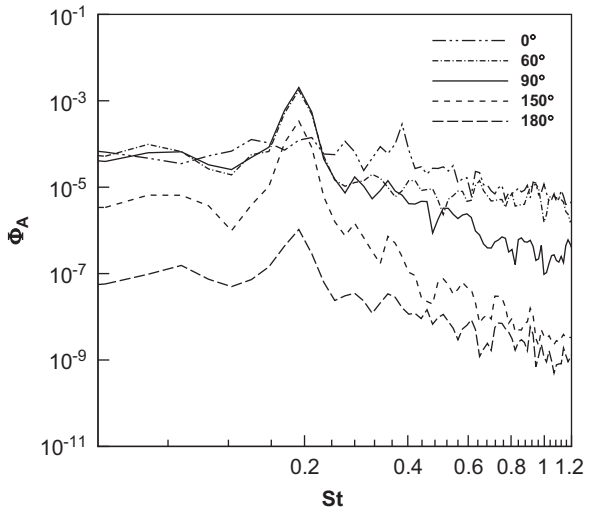

Fig. 6. Auto-spectra of the surface pressure fluctuations over the cylinder.

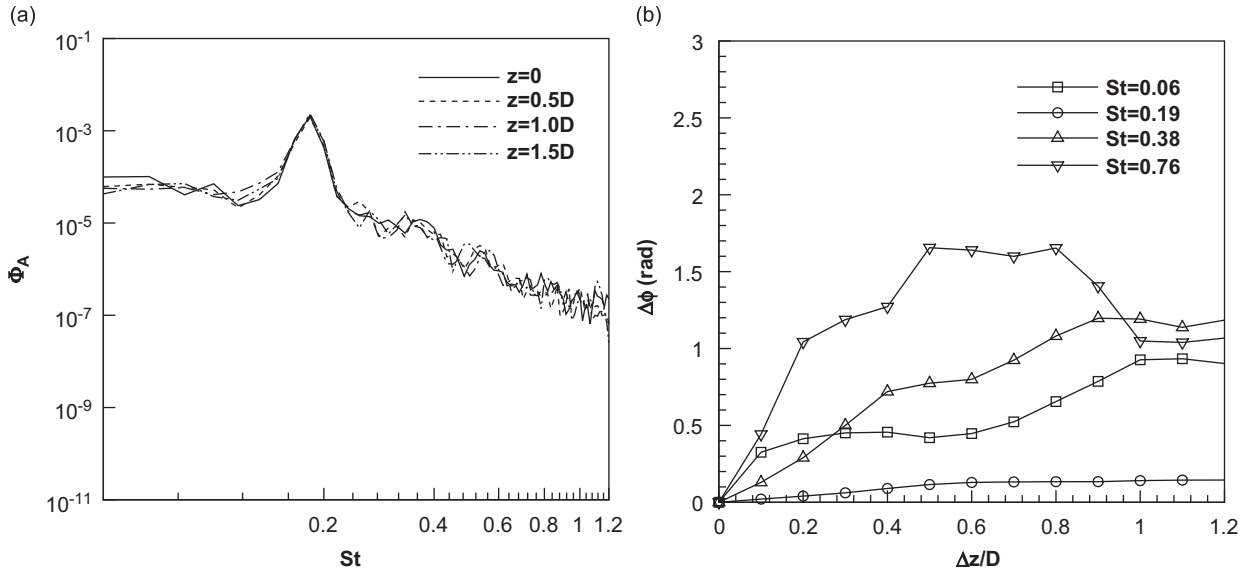

Fig. 7. Spanwise spectral characteristics: (a) auto-spectra of the surface pressure fluctuations; (b) phase difference determined from the cross-spectra.

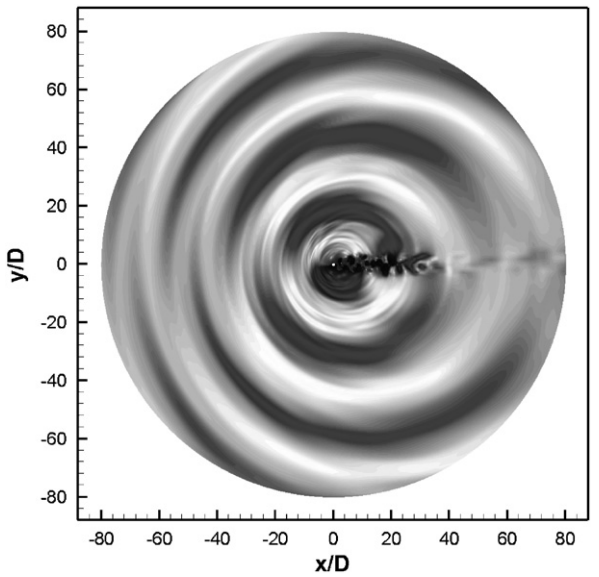

Fig. 8. Instantaneous pressure fluctuation field over the cylinder ($Re_D = 46000$ and $M = 0.21$).

wavelength at the Karman vortex shedding frequency, $St = 0.19$ is expected to be approximately $25D$ at $M = 0.21$. So, meshes are distributed such that waves at $St = 1.4$ are to be resolved with 6–7 grid points per acoustic wavelength at $r = 70D$. This is a typical mesh requirement for the sixth-order spatial differencing scheme used in the present study. A minimal acoustic grid spacing at the wall is also set five times larger than the hydrodynamic grid ($0.025D$) so that acoustic calculation can be conducted with the same time step used for the incompressible LES. This is one of the advantages with the hydrodynamic/acoustic splitting method [11] because a synchronous computation can be conducted for flow and acoustics without any time interpolation. It is also mentioned that the spanwise-integrated incompressible LES solution is directly interpolated onto the

acoustic grid, using a bi-linear shape function. This simple interpolation technique maintains the accuracy because the interpolation is conducted from the fine hydrodynamic meshes to the coarse acoustic grids.

Fig. 8 shows the instantaneous pressure fluctuation field ($\Delta p' = \overline{(P+p')} - (P+p')$) calculated by LPCE for the entire acoustic domain. One can clearly see that the tonal waves are the dominant ones compared to the high-frequency waves observed in the near field. This dipole tone is generated by the Karman vortex shedding, while the short waves are emanated from the volume sources (i.e. wake turbulences). A time variation of the pressure fluctuations at $r = 70D$ directly above the cylinder is presented in Fig. 9. The acoustic pressure oscillates at the Karman vortex shedding frequency but certainly not regular as the laminar tone. The directivity pattern of $\Delta p'_{\mathrm{rms}}$ at $r = 70D$ shown in Fig. 10 clearly indicates a dipole but not like the laminar case (i.e. twin circles). The laminar tone characteristics of the cylinder cross flow at $Re_D = 200$ and $M = 0.3$ may be found in Ref. [11].

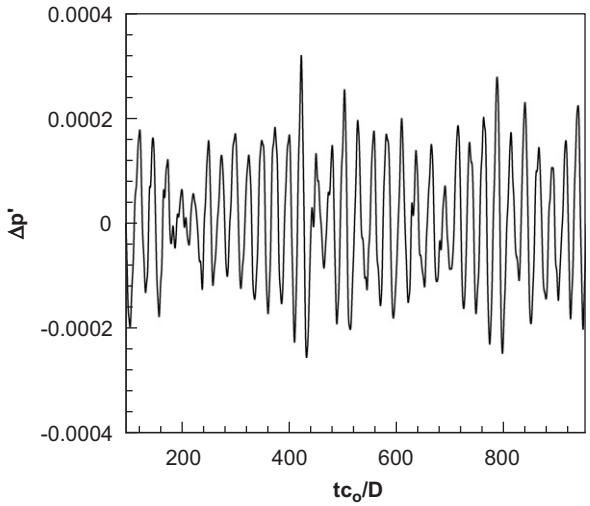

Fig. 9. Time variation of acoustic pressure at $r = 70D$ directly above the cylinder, non-dimensionalized by $\rho_\infty c_\infty^2$.

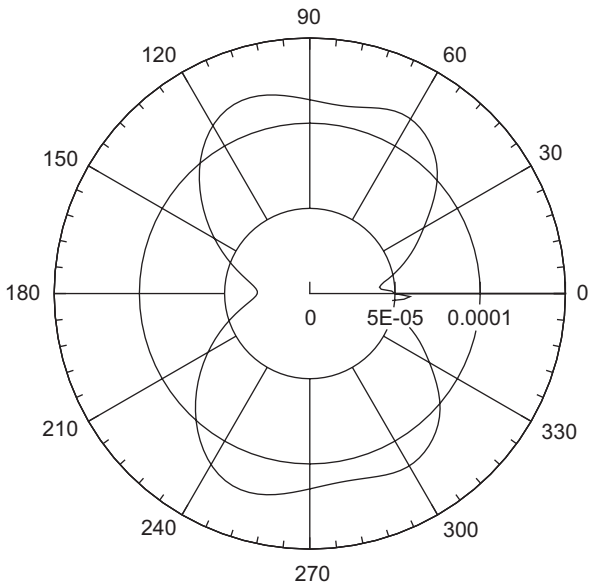

Fig. 10. Directivity pattern of $\Delta p'_{\mathrm{rms}}$ at $r = 70D$, non-dimensionalized by $\rho_\infty c_\infty^2$.

3.3. Far-field SPL for the long span

In experiments [1,24], a far-field sound is measured at $r = 185D$ from the circular cylinder, as shown in Fig. 3, but our computational domain of acoustics is truncated at $r = 80D$ for computational efficiency. Therefore, acoustic pressure at $r = 70D$ (i.e. Kirchhoff surface) is extrapolated to $r = 185D$ by 2D Kirchhoff method, Eq. (11), followed by a 3D spectral acoustic pressure correction with Oberai et al.'s formula, Eq. (10). In order to verify the computational methods, an acoustic power spectral density (PSD) at $r = 185D$ (computed by LPCE with Eqs. (10) and (11)) is compared in Fig. 11 with the Curle's analogy solution. The SPL spectra look quite similar, in overall, including the match of peak at $St \sim 0.19$. Some discrepancy in the high-frequency region (e.g. $0.3 < St < 1.2$) is due to the fact that the volume sources in the wake are not included in the Curle's solution. The LPCE result clearly shows the contributions of the volume sources and also two secondary peaks at $St \sim 0.38$ and 0.56, which are clearly observed in experiment (see Fig. 14).

In order to estimate the far-field SPL of the long span ($L = 30D$), a correction must be taken into account by Eq. (18) (or (19)), considering the acoustic spanwise coherence function, $\gamma'(\Delta z_{ij})$. In the present study, the spanwise coherence function is obtained by dividing the simulated span, $L_s = 3D$ into 30 smaller subsections and applying the Curle's analogy to each subsection (i.e. $0.1D$). The calculated spanwise coherence function (symbols in Fig. 12) is, however, only valid up to $\Delta z = L_s/2 = 1.5D$ because the spanwise periodic boundary condition was used in the present computation. Except at Karman vortex shedding frequency ($St = 0.19$), the coherence functions are rapidly decaying, as Δz increases. So, one can easily fit them with a Gaussian function, $\exp(-\Delta z^2/L_c'^2)$ (solid line in Fig. 12) and determine the coherence length, L_c' for various frequencies. Around $St = 0.19$, the coherence function is so slowly decaying that the fitting may yield an inaccurate estimation of L_c'. But its sensitivity to the SPL is found rather weak. Discussion on the sensitivity of L_c' to $\mathrm{SPL}_c(\omega)$ will be made later in this section.

It would be also useful to replace γ_{ij}' by the spanwise coherence function of the surface pressure at a point of interest because of its easiness in measurement [23,24]. The acoustic spanwise coherence function, γ_{ij}' is actually related to the spanwise coherence function of the integrated surface pressure, as described in Eq. (22). In the present problem, the integrated surface pressure will be dominated by the surface pressure fluctuations at the cylinder top ($\theta = 90^\circ$) because both the directional cosine ($\vec{r} \cdot \hat{n}$) and the surface pressure fluctuations have peaks at this position (see Figs. 3 and 6). The spanwise coherence function of the surface pressure at $\theta = 90^\circ$ is defined as

$$\Gamma_{ij} = \frac{\overline{\mathrm{Re}(\hat{P}_i \hat{P}_j^*)}}{\sqrt{|\hat{P}_i|^2}\sqrt{|\hat{P}_j|^2}}, \tag{23}$$

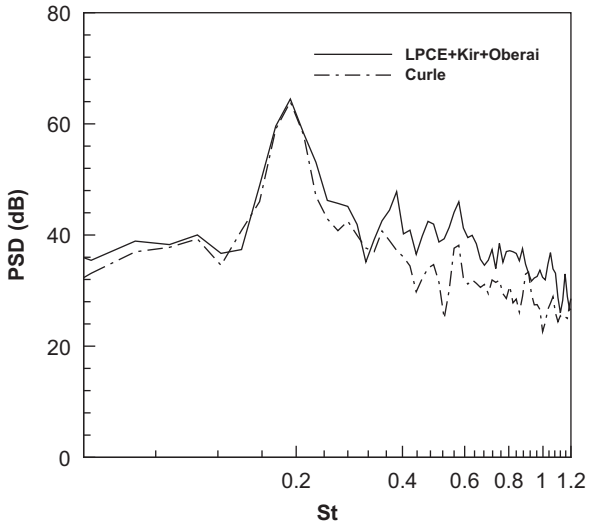

Fig. 11. Power spectral density of acoustic pressure at $r = 185D$ directly above the cylinder for the span, $L_s(= 3D)$.

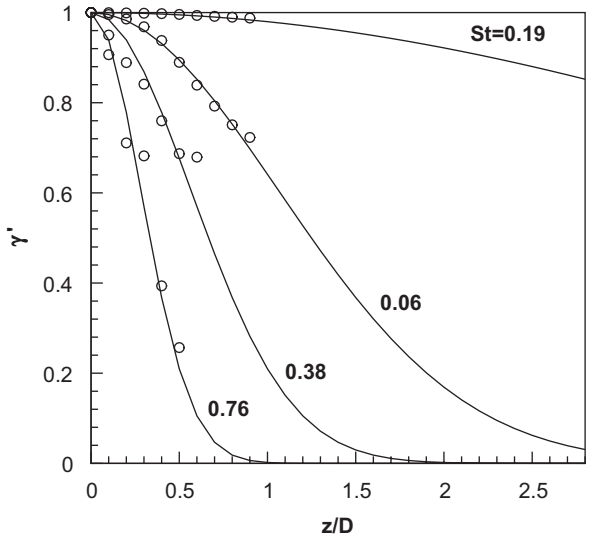

Fig. 12. Spanwise coherence function of the acoustic pressure emitted from the simulated span.

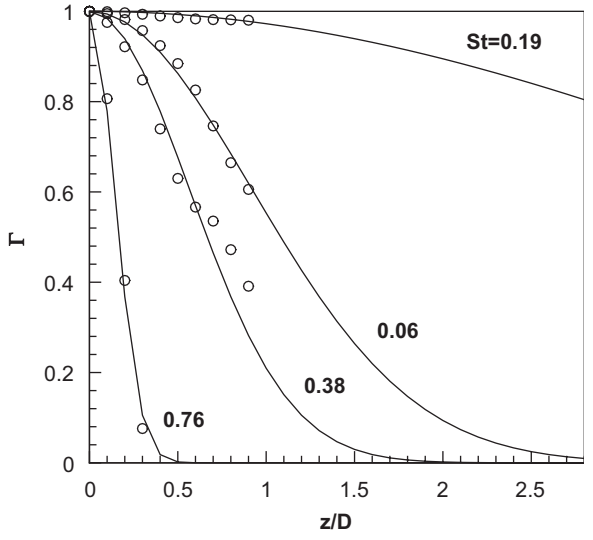

Fig. 13. Spanwise coherence function of the surface pressure over the simulated span ($\theta = 90^\circ$).

where the subscript denotes a subsection within the span. Eq. (23) is now plotted in Fig. 13 (symbols) with the Gaussian function fitted (solid line). At the Karman vortex shedding frequency, the spanwise coherence length is computed as $6D$, which is quite close to the measured value [23,24]. As one can see in Figs. 12 and 13, the spanwise coherence functions, γ'_{ij} and Γ_{ij} (at $\theta = 90^\circ$) look quite similar and in practice, γ'_{ij} could be replaced by Γ_{ij} at a point of interest. The coherence function, Γ_{ij} is often available in the experimental measurements or can be easily computed.

As shown in Figs. 12 and 13, Γ_{ij} is not perfectly the same as γ'_{ij} because it depends on the position and is also problem-dependent. Thereby, the spanwise coherence length determined by the surface pressure may be different in a certain degree from that obtained by the acoustic coherence. The amount of SPL to be corrected for the long span, $\mathrm{SPL}_c(\omega)$ is, however, found not so sensitive to the accuracy of the computed spanwise coherence length. The spanwise coherence lengths, L'_c determined from Figs. 12 and 13 are listed in Table 2. At

Table 2
Computed spanwise coherence lengths

St		0.06	0.19	0.38	0.76
$L_c'(\omega)$	γ'	$1.5D$	$7D$	$0.8D$	$0.4D$
	Γ	$1.3D$	$6D$	$0.8D$	$0.2D$

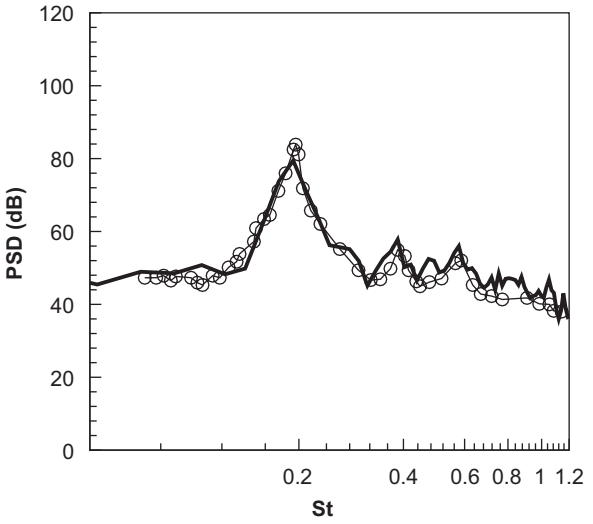

Fig. 14. Sound pressure level spectrum at $r = 185D$ for $L = 30D$; −: present, ○: measurement [1,24].

$St = 0.76$, the coherence length of the surface pressure is smaller by half than that of the acoustic pressure because the surface pressure fluctuations at high frequencies are not strongly noticeable at $\theta = 90^\circ$ (see Fig. 3). At other frequencies, however, only small differences are observed. In most cases, coherence lengths are smaller than $L_s/\sqrt{\pi}(\approx 1.7D)$ and accordingly, 10(dB) is added for correction. Therefore, obtaining the precise values of L_c' is not so critical at these frequencies. The frequencies around $St = 0.19$ (vortex shedding frequency), however, may fall into the most difficult case, i.e. $1/\sqrt{\pi} < L_c'/L_s < N/\sqrt{\pi}$. Because the spanwise coherence lengths are larger than the simulated span, the computed spanwise coherence lengths may not be so accurate. But $\pm 1D$ variations in L_c' correspond to ± 1(dB) in SPL$_c$. Therefore, a reasonably estimated spanwise coherence length may suffice the case. Additionally, in the flow with coherent vortex shedding, the coherence length scale can be fitted with an exponentially decaying function centered at the vortex shedding frequency as $L_c'(\omega) \sim L_0 \exp(-A|\omega - \omega_0|)$, where ω_0 is the vortex shedding frequency and L_0 is the coherence length at the vortex shedding frequency [26]. For the broadband part of the spectrum ($\omega \gg \omega_0$), another exponential function can be used to fit L_c', i.e. $L_c'(\omega) \sim B \exp(-C * \omega)$. Such fittings can make easier to evaluate SPL$_c$ with Eq. (18) or (19) for a wide range of frequencies.

The far-field SPL for $L = 30D$ is finally estimated by Eq. (18) with the spanwise coherence lengths listed in Table 2 (with γ_{ij}'). The acoustic pressure PSD is compared in Fig. 14 with the experimental data measured at the *Ecole Centrale de Lyon* [1,24]. It is shown that the computed SPL spectrum agrees well with the experimental data. One can clearly identify the broadened peak around the Karman vortex shedding frequency, $St = 0.19$ and also the secondary peaks at $St = 0.38$ and 0.57, all of which well coincide with the measured data. This study shows that the present computational methodology is consistent and capable of predicting the aerodynamic noise of long-span bodies with reasonable accuracy.

4. Conclusive remarks

A computational methodology is proposed for aerodynamic noise prediction of long-span bodies at low Mach numbers. Accuracy of the present method is assessed for broadband noise (with a broadened tone) from a flow with $Re_D = 4.6 \times 10^4$ and $M = 0.21$, past a circular cylinder of 30 cylinder-diameter span. The computed aerodynamic coefficients of the cylinder (St, C_L and C_D in rms and averaged values) and its far-field SPL for the long span are found in excellent agreement with the experimental measurements, indicating that the proposed method is consistent and accurate. It is also numerically shown that the acoustic spanwise coherence function can be replaced by the spanwise coherence function of the surface pressure at a point of interest and also that SPL correction for the long span is not so critically sensitive to the accuracy of the computed spanwise coherence lengths. When $1/\sqrt{\pi} < L_c'/L_s < N/\sqrt{\pi}$, for example, it is found that $\pm 1D$ variations in L_c' correspond to $\pm 1(\mathrm{d}B)$ in $\mathrm{SPL}_c(\omega)$.

References

[1] J. Boudet, D. Casalino, M.C. Jacob, P. Ferrand, Prediction of sound radiated by a rod using large eddy simulation, AIAA-Paper 2003-3217, 2003.
[2] F. Perot, J.M. Auger, H. Giardi, X. Gloerfelt, C. Baily, Numerical prediction of the noise radiated by a cylinder, AIAA-Paper 2003-3240, 2003.
[3] X. Gloerfelt, C. Bogey, C. Baily, LES of the noise radiated by a flow over a rectangular cavity, *Proceedings of LES for Acoustics*, DGLR-Report 2002-03, 2002.
[4] M. Terracol, E. Manoha, C. Herrero, P. Sagaut, Airfoil noise prediction using large eddy simulation, Euler equation and Kirchhof integral, *Proceedings of LES for Acoustics*, DGLR-Report 2002-03, 2002.
[5] C. Baily, C. Bogey, D. Juve, Computation of flow noise using source terms in linearized Euler equations, AIAA-Paper 2000-2047, 2000.
[6] R. Ewert, W. Schröder, Acoustic perturbation equations based on flow decomposition via source filtering, *Journal of Computational Physics* 188 (2003) 365–398.
[7] R. Ewert, W. Schröder, On the simulation of trailing edge noise with a hybrid LES/APE method, *Journal of Sound and Vibration* 270 (2004) 509–524.
[8] J.C. Hardin, D.S. Pope, An Acoustic/Viscous Splitting Technique for Computational Aeroacoustics, *Theoretical and Computational Fluid Dynamics* 6 (1994) 323–340.
[9] W.Z. Shen, J.N. Sorenson, Aeroacoustics modeling of low-speed flow, *Theoretical and Computational Fluid Dynamics* 13 (1999) 1057–1064.
[10] S.A. Slimon, M.C. Soteriou, D.W. Davis, Computational aeroacoustics simulations using the expansion about incompressible flow approach, *AIAA Journal* 37 (4) (2000) 409–416.
[11] J.H. Seo, Y.J. Moon, Perturbed compressible equations for aeroacoustic noise prediction at low Mach numbers, *AIAA Journal* 43 (8) (2005) 1716–1724.
[12] J.H. Seo, Y.J. Moon, Linearized perturbed compressible equations for low Mach number aeroacoustics, *Journal of Computational Physics* 218 (2006) 702–719.
[13] J.N. Scott, A.R. Pilon, A.S. Lyrintzis, T.J. Rozmajzl, A numerical investigation of noise from a rectangular jet, AIAA-Paper 1997-285, 1997.
[14] A.A. Oberai, F. Roknaldin, T.J.R. Hughes, Trailing-edge noise due to turbulent flows, Technical report, Report No. 02-002, Boston University, 2002.
[15] C. Kato, A. Iida, Y. Takano, Fujita, H., and Ikegawa, M., Numerical prediction of aerodynamic noise radiated from low Mach number turbulent wake, AIAA-Paper 93-145, 1993.
[16] S. Szepessy, P.W. Bearman, Aspect ratio and end plate effect on vortex shedding from a circular cylinder, *Journal of Fluid Mechanics* 234 (1992) 191–217.
[17] S. Szepessy, On the spanwise correlation of vortex shedding from a circular cylinder at high subcritical Reynolds number, *Physics of Fluid* 6 (7) (1994) 2406–2416.
[18] S.K. Lele, Compact finite difference schemes with spectral-like resolution, *Journal of Computational Physics* 103 (1992) 16–42.
[19] D. Gaitonde, J.S. Shang, J.L. Young, Practical aspects of high-order numerical schemes for wave propagation phenomena, *International Journal of Numerical Method in Engineering* 45 (12) (1999) 1849–1869.
[20] E. Manoha, C. Delahay, P. Sagaut, I. Mary, S. Khelil, P. Guillen, Numerical prediction of unsteady flow and radiated noise from a 3D lifting airfoil, AIAA-Paper 2001-2133, 2001.
[21] J.H. Seo, Y.J. Moon, Prediction of low Mach number turbulent flow noise using the splitting method, AIAA-Paper 2004-2860, 2004.
[22] R. Ewert, M. Meinke, W. Schröder, Computation of trailing edge noise of a 3D lifting airfoil in turbulent subsonic flow, AIAA-Paper 2003-3114, 2003.

[23] D. Casalino, M. Jacob, Prediction of aerodynamic sound from circular rods via spanwise statistical modelling, *Journal of Sound and Vibration* 262 (4) (2003) 815–844.
[24] M.C. Jacob, J. Boudet, D. Casalino, M. Michard, A rod-airfoil experiments as a benchmark for broadband noise modeling, *Theoretical and Computational Fluid Dynamics* 19 (3) (2005) 171–196.
[25] M.R. Visbal, D.P. Rizzetta, Large-eddy simulation on curvilinear grids using compact differencing and filtering schemes, *Journal of Fluid Engineering* 124 (12) (2002) 836–847.
[26] M. Roger, S. Moreau, A. Guèdel, Vortex-shedding noise and potential-interaction noise modeling by a reversed Sears' problem, AIAA-Paper 2006-2607, 2006.